Energy & Environmental Science

PAPER

View Article Online
View Journal

Published on 18 July 2025. Downloaded by Yunnan University on 8/2/2025 10:13:48 PM.

Cite this: DOI: 10.1039/d5ee02236c

Interfacial gradient engineering synergized with self-adaptive cathodic defense for durable Zn-ion batteries

Quan Zong, †*[abc] Xuelian Liu,†[a] Qilong Zhang, *[b] Qiaoling Kang, [a]
Fan Wang,[a] Guoying Wei[a] and Anqiang Pan *[c]

Received 22nd April 2025,
Accepted 17th July 2025

DOI: 10.1039/d5ee02236c

rsc.li/ees

The undesirable electrode/electrolyte interfaces, resulting in severe parasitic reactions and uncontrolled dendrite growth at the Zn anode, as well as cathode dissolution, significantly hinder the practical application of aqueous zinc-ion batteries. Herein, a diethyl phosphoramidate (DP) additive was proposed to regulate the interfacial chemistry at both anode and cathode. DP molecules disrupt the hydrogen bond network and suppress interfacial pH fluctuations, effectively reducing water activity and inhibiting side reactions. DP molecules preferentially adsorb onto the Zn surface, facilitating the formation of a robust crystalline–amorphous hybrid solid electrolyte interphase (SEI) composed of ZnS, Zn_3N_2, and $Zn_3(PO_4)_2$, which not only enhances Zn^{2+} transport kinetics but also homogenizes the zinc ions deposition. The dissolution of a vanadium-based cathode is alleviated, and the DP-rich cathode electrolyte interphase promotes the ion desolvation. As a result, Zn||Zn symmetric cells achieve extended cycling life, while Zn||Cu asymmetric cells exhibit high coulombic efficiencies. Additionally, both Zn||$NH_4V_4O_{10}$ full cells and pouch cells demonstrate improved cycling stability.

Broader context

Aqueous zinc-ion batteries (ZIBs) have garnered attention as next-generation energy storage systems, particularly for large-scale grid applications, due to their intrinsic safety, cost-effectiveness, and environmental compatibility. However, the Zn anode still suffers from dendrites and side reactions, and sluggish reaction kinetics and severe dissolution of cathodes limit the discharge capacity and cycling stability. Herein, the molecule DP is introduced to reconstruct the hydrogen bond network, adjust interfacial chemistry, and *in situ* form a robust crystalline and amorphous hybrid solid electrolyte interphase, thereby suppressing side reactions, accelerating desolvation kinetics, and homogenizing Zn deposition. In addition, a self-adaptive DP-rich cathode electrolyte interphase suppresses the dissolution of the vanadium-based cathode and promotes the reaction kinetics. This work presents a new perspective on electrolyte additives compatible with both the cathode and anode for high-performance ZIBs.

Introduction

The demand for sustainable and high-performance energy storage systems has spurred intensive research into aqueous zinc-ion batteries (ZIBs), which are recognized for their cost-effectiveness, environmental friendliness, and inherently high safety.[1,2] Compared to conventional lithium-ion batteries, ZIBs employ non-flammable aqueous electrolytes with high ionic conductivity and Zn metal anodes with a high theoretical capacity (820 mAh g^{-1}) and low redox potential (−0.76 V *vs.* the standard hydrogen electrode).[3–5] However, the practical application of ZIBs is severely hindered by the instability of electrode/electrolyte interfaces.[6] Uncontrolled dendrite growth at the Zn anode not only degrades electrochemical performance but also leads to short circuits.[7,8] The presence of water molecules in the electrolyte facilitates parasitic reactions, including hydrogen evolution reaction and corrosion.[9,10] In addition, the loss of structural integrity of the active materials due to dissolution in an auqeous environment still limits the electrochemical performance of cathodes.[11,12]

Various strategies have been explored to address these interfacial challenges, including the use of artificial interfacial layers, modifications to the electrode structures, adjustments

---

[a] *College of Materials and Chemistry, China Jiliang University, Hangzhou 310018, Zhejiang, People's Republic of China. E-mail: quanzong@cjlu.edu.cn*
[b] *State Key Lab of Silicon and Advanced Semiconductor Materials, Zhejiang University, Hangzhou 310027, Zhejiang, People's Republic of China. E-mail: mse237@zju.edu.cn*
[c] *School of Materials Science & Engineering, Central South University, Changsha 410083, Hunan, People's Republic of China. E-mail: pananqiang@csu.edu.cn*

† These authors contributed equally to this work.

Published on 18 July 2025. Downloaded by Yunnan University on 8/2/2025 10:13:48 PM.

to the separators, and engineering of electrolyte compositions.[13–16] In comparison to *ex situ* strategies, electrolyte additive engineering has gained significant attention owing to its simplicity, cost-effectiveness, and scalability.[17,18] Additives such as highly concentrated electrolytes, organic co-solvents, and functional molecules have been used to alter the solvation structure and interfacial chemistry of Zn anodes, thereby regulating Zn deposition and suppressing parasitic reactions.[19–21] In terms of the cathodes, manganese-based compounds, vanadium-based compounds, and Prussian blue analogs have been developed as high-performance cathode materials for ZIBs.[22,23] However, the dissolution of these cathode materials is commonly observed in aqueous electrolytes, occurring at the electrode–electrolyte interface, primarily driven by the pronounced polarity of water.[24,25] Adding additives to the electrolyte can also efficiently help suppress dissolution and stabilize the structure, thereby improving the capacity and lifespan of the cathode. For example, Mn^{2+} additives could adjust the equilibrium reaction between the electrolyte and the Mn-based cathode to suppress the dissolution of manganese in manganese-based material.[26,27] The dissolution of $VOPO_4$ is inhibited by reducing the water activity in the electrolyte using glucose as a hydrogen bond regulator.[28] However, most electrolyte additives primarily focus on either cathode or anode modification, with limited attention given to simultaneous improvements in both anode and cathode performance. Therefore, it is essential to design electrolyte additives that are compatible with both anodes and cathodes and to thoroughly explore their mechanisms of action.

In this work, we employ diethyl pyrophosphoramide (DP) as a multi-functional electrolyte additive to optimize the interfacial chemistry of the cathode, regulate electrolyte structure, and enable the *in situ* formation of a gradient organic–inorganic hybrid SEI on the anode (Fig. 1). Theoretical calculations and experimental results confirm that DP molecules disrupt the hydrogen bond network of water and preferentially adsorb onto the Zn surface through strong $P{=}O\cdots Zn$ interactions, reducing the water reactivity and homogenizing Zn^{2+} flux. Moreover, interfacial DP molecules participate in the formation of a robust, crystalline–amorphous hybrid SEI on the Zn surface, consisting of ZnS, Zn_3N_2, and $Zn_3(PO_4)_2$, which acts as an ion-permeable yet electronically insulating protective layer. The triple functions of DP molecules effectively prevent dendrite growth and suppress interfacial side reactions. On the cathode side, DP interacts with $NH_4V_4O_{10}$ (NVO) to form a self-adaptive cathode electrolyte interphase (CEI), effectively suppressing V dissolution and accelerating the desolvation process. As a result, Zn||Zn symmetric cells exhibit long cycling stability over 1200 h at 10 mA cm^{-2} with 5 mAh cm^{-2}, while Zn||Cu asymmetric cells achieve an average Coulombic efficiency of 99.7% over 800 cycles. Furthermore, Zn||NVO full cells demonstrate significantly improved cycling stability, highlighting the practical applicability of this electrolyte engineering strategy.

Results and discussion

The $ZnSO_4$ electrolytes containing different concentrations of DP are shown in Fig. S1, with all samples exhibiting a clear and transparent appearance. As the DP content increases, the Raman spectra of the electrolytes display an increased intensity of the characteristic peaks for the DP molecule (Fig. S2), indicating the successful incorporation of DP. The O–H stretching vibration in the range of 3000–3800 cm^{-1} can be deconvoluted into three distinct peaks, corresponding to strong, medium, and weak hydrogen bonds, respectively (Fig. S3).[29] Compared to the DP-0 electrolyte, the introduction of DP leads to a decrease in the proportion of strong hydrogen bonds, accompanied by an increase in medium and weak hydrogen bonds (Fig. 2a). This result suggests that DP effectively interacts with water molecules, disrupting the strong hydrogen-bonding network within the electrolyte, which reduces the activity of H_2O molecules. Fourier transform infrared (FTIR) spectra, presented in Fig. S4, show the $P{=}O$ stretching vibration of DP at 1216 cm^{-1}, which exhibits a gradually increasing peak intensity.[30] As the concentration of DP electrolyte increases, the O–H stretching vibration band exhibits a shift toward higher wavenumbers (Fig. 2b), suggesting a disruption in the intrinsic

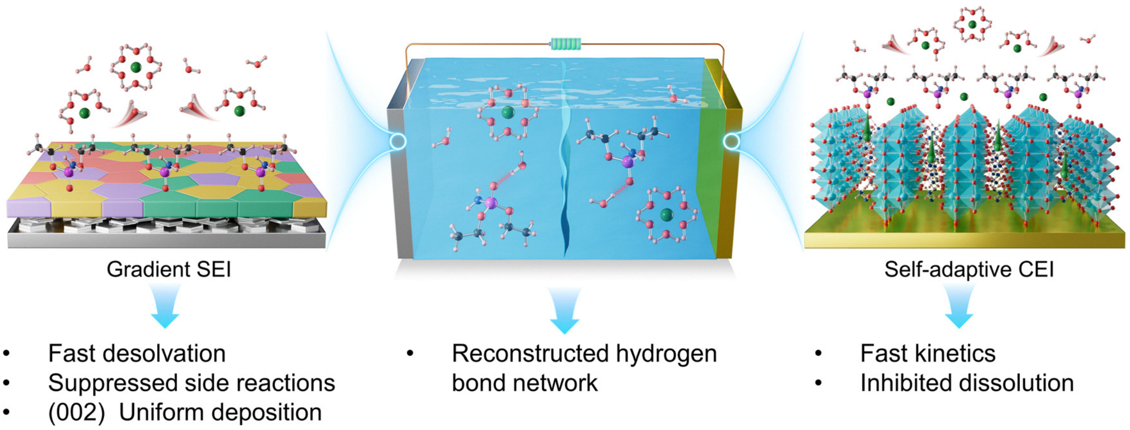

Fig. 1 Schematic illustration of the effect mechanism of the DP additive on the bulk electrolyte and electrode/electrolyte interfaces.

Published on 18 July 2025. Downloaded by Yunnan University on 8/2/2025 10:13:48 PM.

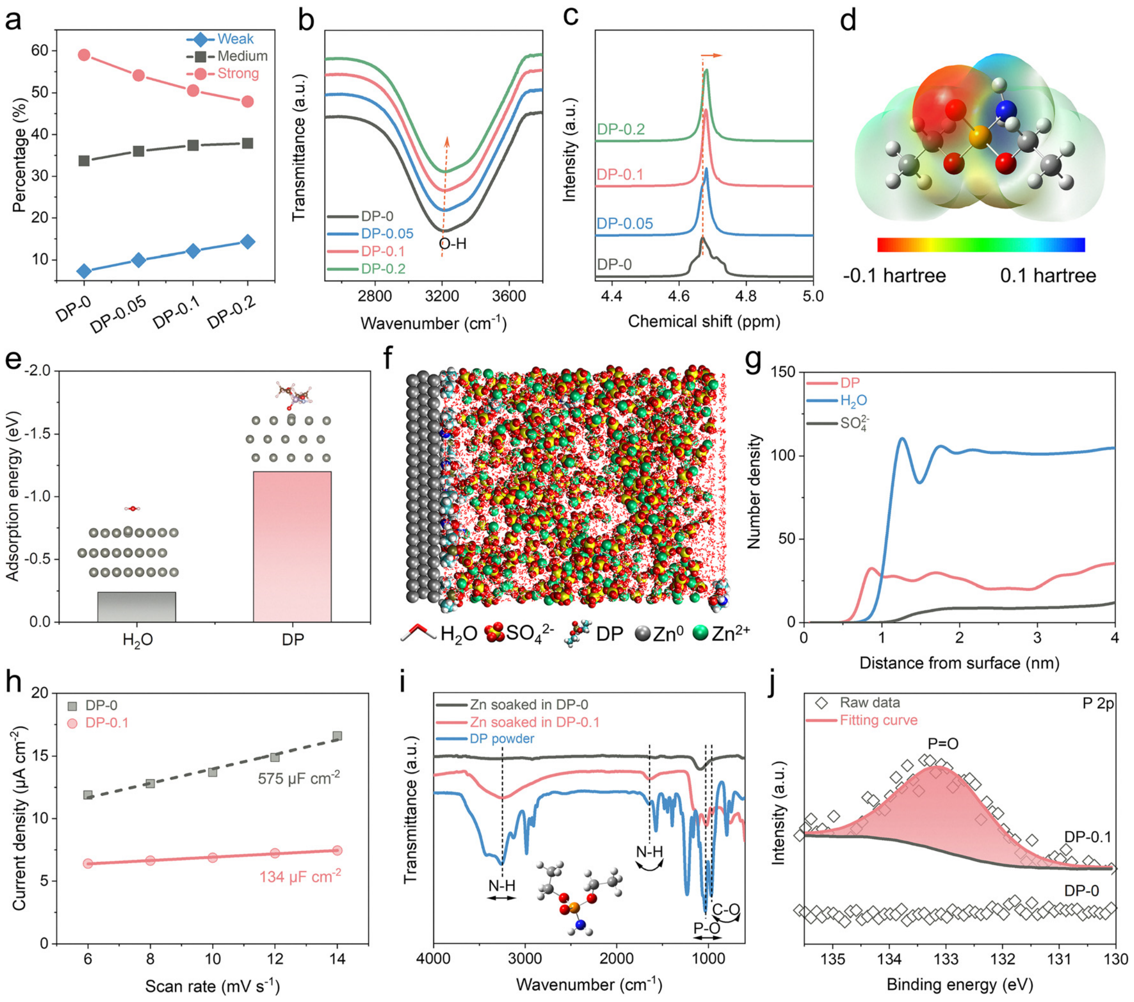

Fig. 2 Characterizations of electrolyte structure and adsorption behavior of DP molecules. (a) Ratios of strong, medium, and weak H bonds in various electrolytes. (b) FTIR and (c) NMR spectra of electrolytes with different concentrations of DP. (d) ESP mapping of the DP molecule. (e) Adsorption energy of H_2O and DP on Zn (002) plane. (f) MD simulations of the interface region in the DP-0.1 system. (g) Relative concentration distribution of DP, H_2O and SO_4^{2-} species in the interface region. (h) EDLC for Zn anode in DP-0 and DP-0.1 electrolytes. (i) FTIR and (j) P 2p XPS spectra of immersed Zn foils in DP-0 and DP-0.1 electrolytes.

hydrogen-bonding network among water molecules due to competitive hydrogen bonding between DP and H_2O molecules. The ^{1}H nuclear magnetic resonance (NMR) spectra (Fig. 2c) show the O–H bond peak shifting to a higher field with increasing DP concentration, supporting the formation of hydrogen bonds between DP and H_2O.[31] The characteristic peaks of DP exhibit the same trend of change (Fig. S5) with those in Raman and FTIR spectra. These results demonstrate the disruption and reconstruction of hydrogen bonding networks after the introduction of DP, which reduces the activity of free H_2O molecules, possibly contributing to the suppression of side reactions. Besides, a slight increase in ionic conductivity is observed with rising DP concentration (Fig. S6). This is because the reconstructed hydrogen-bonding network results in a slight reduction in viscosity (Fig. S7), and the migration of SO_4^{2-} is suppressed, which is consistent with recent studies. The pH increases with the addition of DP (Fig. S8), due to the interaction between weakly basic functional groups and protons. Based on the cycling performance of Zn||Zn symmetric cells with different electrolytes (Fig. S9), the optimal concentration of DP is determined to be 0.1 M. As shown in Fig. S10, the Zn-ion transference number ($t_{Zn^{2+}}$) in DP-0.1 electrolyte is calculated to be 0.61, which is larger than that for the DP-0 electrolyte ($t_{Zn^{2+}}$ = 21). This could be attributed to the presence of zincophilic sites within DP, which facilitate Zn^{2+} diffusion and effectively mitigate SO_4^{2-} aggregation, thereby improving ion transport dynamics.[32]

The electrostatic potential (ESP) mapping of DP (Fig. 2d) shows that the P=O group exhibits electronegativity, suggesting a strong chemical affinity between the DP molecule and the Zn metal surface. As shown in Fig. 2e, density functional theory (DFT) calculations reveal the adsorption energy of DP and H_2O on the Zn(002) crystal planes. The adsorption energy of DP is calculated to be −1.19 eV, which is more negative than that of H_2O (−0.24 eV), confirming the preferential adsorption of DP over water molecules on the Zn surface. To gain deeper insight

Published on 18 July 2025. Downloaded by Yunnan University on 8/2/2025 10:13:48 PM.

into the interfacial structure and species distribution, molecular dynamics (MD) simulations were performed on Zn interfaces in DP-0 and DP-0.1 systems (Fig. 2f and Fig. S11). DP molecules maintain a high density at the Zn anode interface. At the same time, the distribution of H_2O and SO_4^{2-} on the surface of Zn is significantly decreased by the DP (Fig. 2g), indicating that the DP molecules accumulate on the electrode surface, effectively excluding active H_2O molecules from the Zn surface and preventing them from interacting with the Zn anode. On the contrary, significant enrichment of H_2O, SO_4^{2-}, and Zn^{2+} is observed at the interface in the DP-0 electrolyte (Fig. S12 and S13), which promotes the side reaction of HER or surface corrosion, and the formation of byproducts. The electric double-layer capacitance (EDLC) of the Zn electrode was determined through cyclic voltammetry (CV) measurements conducted at varying scan rates (Fig. S14). Based on the fitting results, the Zn electrode exhibits an EDLC of 575 μF cm^{-2} in the DP-0 electrolyte, which reduces to 134 μF cm^{-2} after the addition of 0.1 M DP (Fig. 2h). The lower EDLC is attributed to the interfacial adsorption of the larger DP molecules instead of water, resulting in an expanded electrochemical double layer. The differential capacitance of Zn in an aqueous solution is depicted in Fig. S15. It is found that the addition of DP to the electrolyte results in a decrease in interfacial capacitance, indicating that the DP molecules are readily adsorbed at the electrode/electrolyte interface. After soaking the Zn foil in the two electrolytes, the FTIR spectrum of the foil in DP-0.1 displays N–H, P–O and C–O peaks that are absent in DP-0 electrolyte, indicating the effective adsorption of DP molecules on the Zn metal surface (Fig. 2i). The P 2p, N 1s and O 1s X-ray photoelectron spectroscopy (XPS) spectra of the soaked Zn further confirm the adsorbed DP molecules (Fig. 2j and Fig. S16, S17).

DFT calculations were conducted to compare the energy levels of lowest unoccupied molecular orbital (LUMO) and highest occupied molecular orbital (HOMO) of DP and H_2O. The results (Fig. 3a) reveal that the DP molecule exhibits a lower LUMO energy level (−0.93 eV) than H_2O (1.014 eV), indicating its superior electron-accepting ability and higher chemical reactivity, which possibly results in the *in situ* transformation into SEI layers.[33] Transmission electron microscopy (TEM) was performed to characterize the structure of the SEI layer. A transparent SEI layer with a thickness of approximately 15 nm is observed in the DP-0.1 electrolyte compared to that in the DP-0 electrolyte (Fig. S18). As shown in high-resolution TEM (Fig. 3b), the distinct lattice fringes correspond to (332) and (321) planes of Zn_3N_2, (110) plane of ZnS, and (−131) and (021) planes of $Zn_3(PO_3)_2$.[34,35] Amorphous regions are distributed throughout the SEI layer. The chemical composition of the SEI layer was further investigated using XPS coupled with Ar^+ sputtering. The S 2p spectrum displayed signals of SO_4^{2-} (≈169.7 eV), SO_3^{2-} (≈168.6 eV), and ZnS (≈162.0 eV) (Fig. 3c).[36,37] The SO_3^{2-} and ZnS were the decomposition products of $ZnSO_4$ salts. As the depth of Ar^+ sputtering increased, the signals of ZnS significantly increased, indicating that the ZnS component is mainly distributed in the inner layer of the SEI. The N 1s spectrum revealed the presence of N–C (≈400.0 eV) and N–Zn (≈398.8 eV) bonds, which were attributed to the DP molecules and the adsorption of DP onto the Zn anode.[38] With the increase of sputtering depth, the signal peaks associated with Zn_3N_2 (398 eV) remain unchanged, suggesting the Zn_3N_2 appears across the SEI (Fig. 3d). For the P 2p spectra (Fig. 3e), the peaks at 134.6 and 133.9 eV are attributed to PO_3 and $Zn_3(PO_4)_2$, respectively. The PO_3 component possesses the highest content on the surface due to the adsorption of DP.[29] After sputtering, the $Zn_3(PO_4)_2$ can still be observed with strong signals, which demonstrates that $Zn_3(PO_4)_2$ is enriched in the entire SEI. These findings demonstrate that a SEI layer composed of Zn_3N_2, $Zn_3(PO_4)_2$, and ZnS, as well as amorphous species, was formed from the interfacial adsorbed DP due to its high electrochemical reactivity, which is consistent with the HRTEM results.

Wettability measurements (Fig. 3f) reveal a decrease in the contact angle between the electrolyte and the Zn anode from 85.6° to 79.5° after the introduction of DP, which could be attributed to the strong molecular affinity between DP and the Zn anode, confirming the strong adsorption capability of DP molecules on the Zn surface. After soaking Zn foils in the electrolytes, the Zn foil in the DP-0.1 electrolyte exhibits high hydrophobicity due to the hydrophobic ethoxy groups ($-OCH_2CH_3$) being oriented towards the electrolyte. In contrast, the smaller contact angle of Zn foil in DP-0 electrolyte is attributed to formation of byproducts.[39] Based on the above comprehensive analyses, the effects of DP adsorption layer and specific compositions and distributions of the SEIs have been determined, as illustrated in Fig. 3g. DP molecules are preferentially adsorbed onto the surface of zinc anode and decompose *in situ* to build an organic/inorganic composite SEI layer. The DP adsorption layer and SEI prevent direct contact between active water and the Zn anode, thereby suppressing water-related side reactions. The organic component enables the SEI layer to possess sufficient rigidity and flexibility to accommodate the volume changes caused by plating/stripping. The inorganic components of ZnS, $Zn_3(PO_4)_2$, and Zn_3N_2, as fast-ionic conductors, facilitate the migration of Zn^{2+} and induce uniform deposition.

In situ pH measurements were conducted to evaluate the stabilizing effect of adsorption and SEI layer on interfacial pH fluctuations during the Zn stripping/plating process at a high current density of 10 mA cm^{-2} (Fig. 3h). During deposition, the electric field drives OH^- toward the electrode surface and repels H^+ from the interface, leading to the high pH. Upon reversal of the field, the anodic potential expels OH^- from the interface and promotes H^+ accumulation, thereby lowering the pH. The pH variation in DP-0 electrolyte was larger than that in DP-0.1 electrolyte, which can be attributed to severe parasitic reactions leading to the continuous consumption of protons at the unstable Zn/electrolyte interface in DP-0 electrolyte. Tafel polarization measurements (Fig. S19) reveal that the corrosion potential of the Zn anode in DP-0 electrolyte was −0.993 V, whereas in DP-0.1 electrolyte, it shifted positively to −0.976 V. The corresponding corrosion current densities in DP-0 electrolyte and DP-0.1 electrolyte were 1.93 mA cm^{-2} and 0.29 mA cm^{-2},

This journal is © The Royal Society of Chemistry 2025

Published on 18 July 2025. Downloaded by Yunnan University on 8/2/2025 10:13:48 PM.

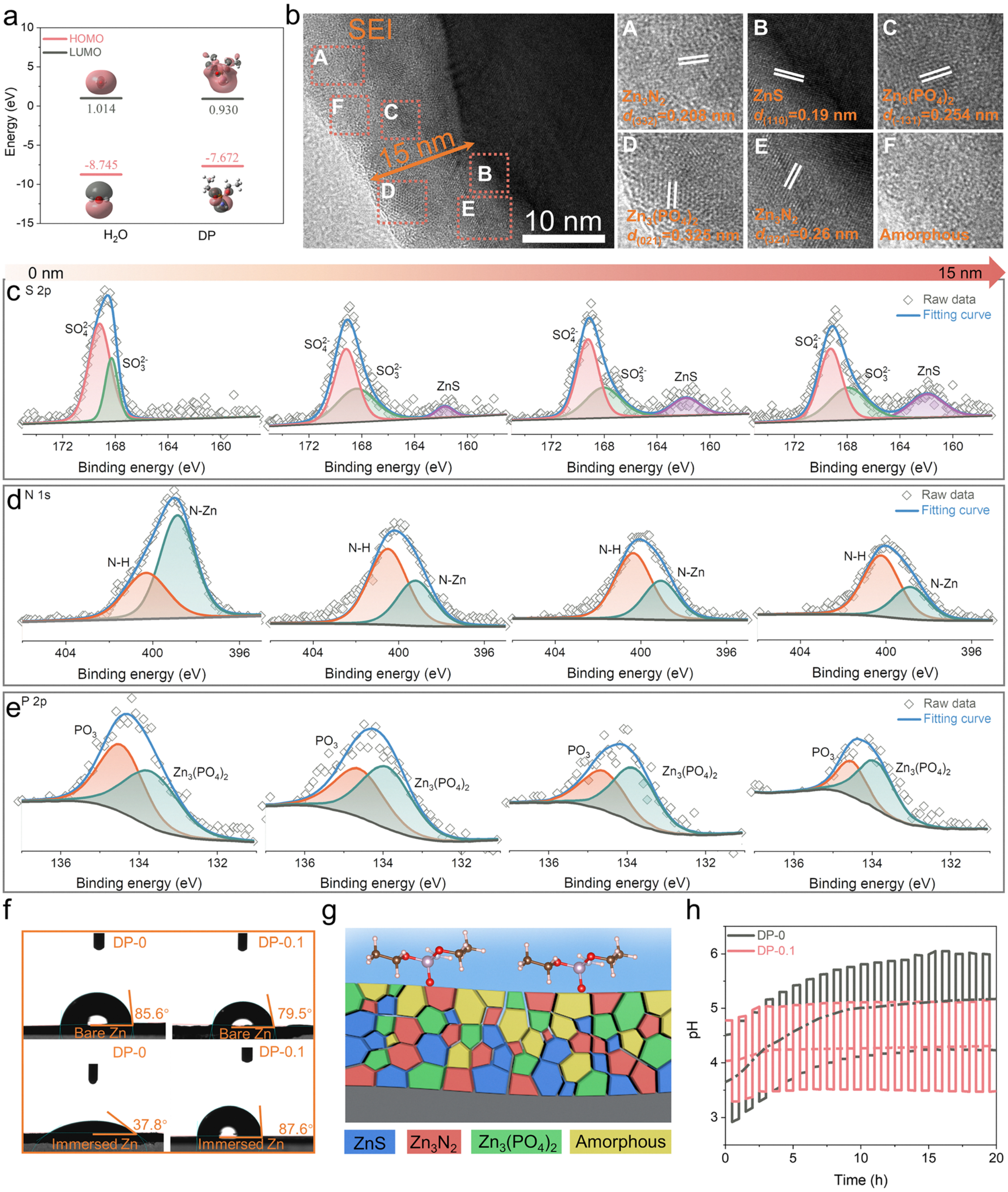

Fig. 3 Study on the SEI and its effects. (a) LUMO and HOMO energy levels of DP and H_2O molecules. (b) TEM and HRTEM images of deposited Zn. In-depth XPS spectra of (c) S 2p, (d) N 1s, and (e) P 2p of the Zn anode after cycling. (f) Contact angles of DP-0 and DP-0.1 electrolytes on bare Zn anode and cycled Zn anode. (g) Schematic diagram of the chemical composition and distribution of SEI. (h) pH evolution of DP-0 and DP-0.1 electrolytes during cycling.

respectively, indicating an improved resistance to corrosion with the addition of DP. Linear sweep voltammetry (LSV) results further demonstrate that the hydrogen evolution reaction (HER) overpotential in DP-0.1 electrolyte reached −1.806 V at −10 mA cm^{-2} (Fig. S20), which is higher than that in DP-0 electrolyte (−1.741 V), suggesting the suppressed HER.[40] Scanning electron microscopy (SEM) images of Zn foils immersed in different electrolytes for 7 days exhibit that the Zn foil surface in DP-0.1 electrolyte displays a smooth and flat morphology without byproduct formation, while zinc foil in DP-0 electrolyte shows a heterogeneous surface with abundant corrosion byproducts (Fig. S21). The X-ray diffraction (XRD) pattern of the immersed Zn foil in DP-0 electrolyte displays the characteristic diffraction of $Zn_4SO_4(OH)_6{\cdot}nH_2O$ (ZSH), a common corrosion byproduct of zinc.[41] In contrast, the zinc foil from the DP-0.1 electrolyte shows only the characteristic peaks of metallic Zn,

Published on 18 July 2025. Downloaded by Yunnan University on 8/2/2025 10:13:48 PM.

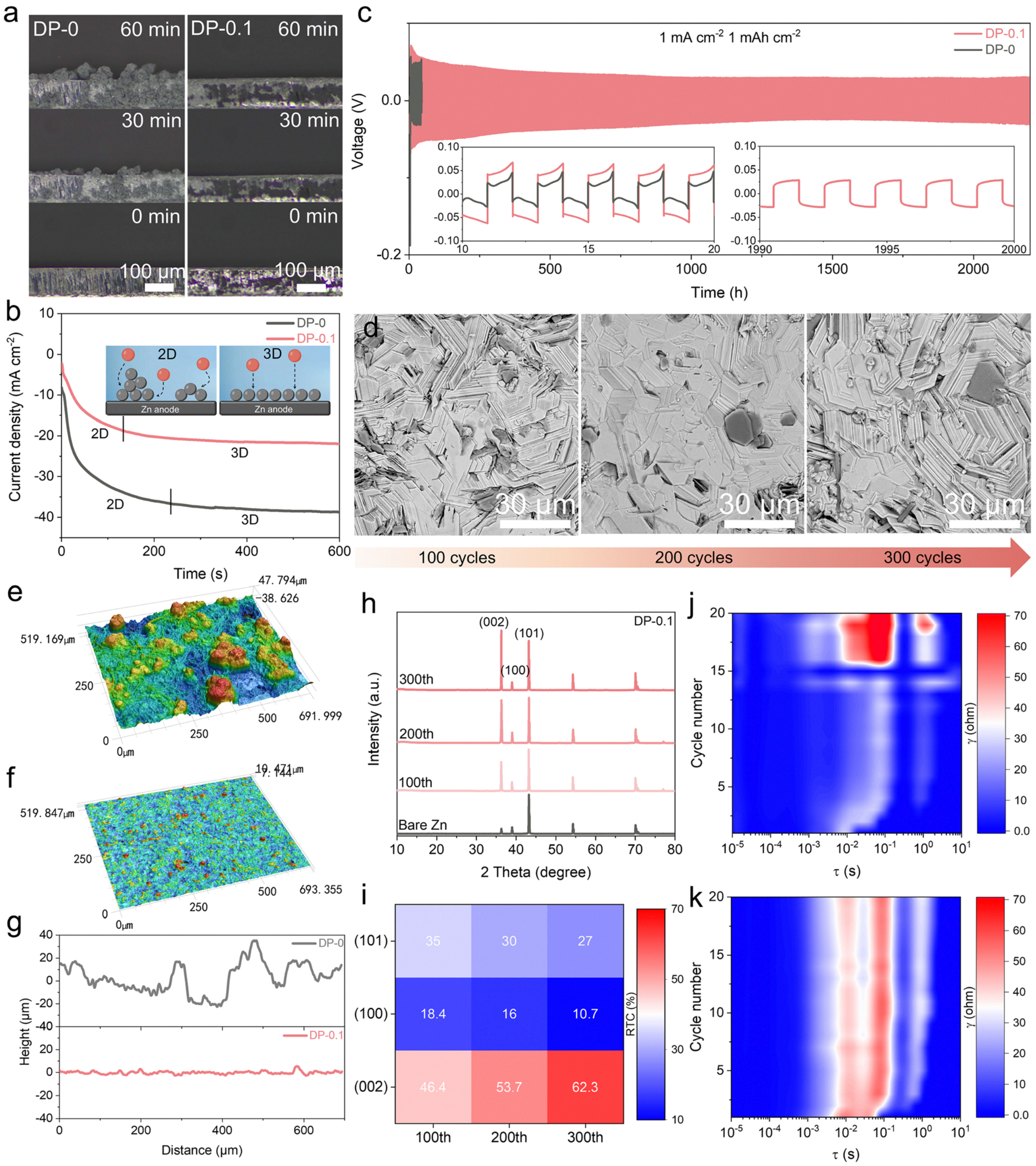

Fig. 4 The interface and deposition behavior. (a) *Operando* optical microscope images of the deposition on Zn anodes in DP-0 and DP-0.1 electrolytes at 5 mA cm^{-2}. (b) CA curves of Zn anode in DP-0 and DP-0.1 electrolytes. (c) Cycling performance of Zn||Zn cells with DP-0 and DP-0.1 electrolytes at 1 mA cm^{-2} and 1 mAh cm^{-2}. (d) SEM images of Zn anodes after 100, 200, and 300 cycles. (e) and (f) CLSM images of Zn anodes after 50 cycles in DP-0 and DP-0.1 electrolytes. (g) Corresponding surface roughness curves. (h) XRD patterns of bare Zn and Zn anodes after 100, 200, and 300 cycles in DP-0.1 electrolyte. (i) Corresponding RTC of Zn anodes. *In situ* DRT plots of Zn||Zn symmetric cells with (j) DP-0 and (k) DP-0.1 electrolytes in the first 20 cycles.

with no evidence of ZSH formation (Fig. S22). These results further confirm the efficacy of the DP additive in preventing byproduct accumulation on the zinc foil surface. The role of SEI on Zn^{2+} desolvation was further determined by the activation energy (E_a) *via* electrochemical impedance spectroscopy (EIS) plots at different temperatures based on the Arrhenius equation (Fig. S23).[42,43] The DP-0.1 electrolyte exhibits a lower E_a value of 13.6 kJ mol^{-1} compared to 23.6 kJ mol^{-1} in DP-0 electrolyte, indicating that the optimized interface facilitates Zn^{2+} desolvation and enhances ion transport kinetics.

As illustrated in Fig. 4a, *in situ* optical microscopy was used to track the evolution of the Zn electrode interface during electrodeposition at 5 mA cm^{-2} in both DP-0 and DP-0.1 electrolytes. In the DP-0 electrolyte, small protrusions rapidly emerge on the Zn surface and progressively grow into dendritic structures over time, indicating an inhomogeneous Zn deposition process. In contrast, Zn deposition in DP-0.1 electrolyte exhibits a uniform, dense morphology throughout the plating period, suggesting that the DP layer and SEI promote homogeneous nucleation and growth. Chronoamperometry (CA)

Published on 18 July 2025. Downloaded by Yunnan University on 8/2/2025 10:13:48 PM.

curves in Fig. 4b display an increased current density in DP-0 electrolyte, suggesting the 2D diffusion process of Zn^{2+}, leading to the random Zn^{2+} nucleation and the dendrite formation. Conversely, in DP-0.1 electrolyte, the Zn deposition rapidly stabilizes into a steady 3D diffusion process, characterized by a lower and more stable current density, promoting a uniform Zn deposition layer. The relationship between grain radius (r) and nucleation overpotential (η) can be described as: $r = 2\gamma V_m/F|\eta|$, where γ represents the surface energy of the electrode/electrolyte interface, V_m is the molar volume of Zn, and F is the Faraday constant.[44] As shown in Fig. S24, the nucleation overpotential in DP-0.1 electrolyte was slightly higher than that in DP-0 electrolyte. The increased nucleation overpotential promotes the formation of smaller nuclei and suppresses the dendrite growth.

Fig. 4c and Fig. S25 show the cycling tests of Zn||Zn symmetric cells with different electrolytes at 1 mA cm^{-2} and 1 mAh cm^{-2}. The cell with DP-0.1 electrolyte exhibits a long lifetime of 2200 h, while the cell with DP-0 electrolyte experiences a short circuit after only 40 h. The increased overpotential of the symmetric cell is attributed to the adsorption of DP on the Zn metal surface, which contributes to the small nucleation size and uniform deposition (Fig. S26).[45,46] SEM images of the Zn electrode in the DP-0.1 electrolyte after various cycling are revealed in Fig. 4d. After 100 cycles, the Zn electrode in the DP-0.1 electrolyte maintains a smooth, uniform surface with densely packed hexagonal Zn flakes. As cycling proceeds, Zn deposition evolves *via* a layer-by-layer mechanism that fosters the formation of a (002) textured growth. Even after 300 cycles, the electrode surface remains flat and compact, demonstrating the effective regulation of Zn deposition and suppression of side reactions. In contrast, the Zn electrode in the DP-0 electrolyte demonstrates a disordered stacking of Zn sheets, which eventually evolves into loosely connected dendritic structures (Fig. S27). 3D confocal laser scanning microscopy (CLSM) images (Fig. 4e and f) and corresponding surface roughness curves (Fig. 4g and Fig. S28) display that the Zn electrode in the DP-0 electrolyte after 50 cycles at 1 mA cm^{-2} and 1 mAh cm^{-2} exhibits a rugged morphology with dendritic protrusions and a significant height difference of 68 μm. By contrast, the Zn electrode in the DP-0.1 electrolyte exhibits a smooth surficial morphology without noticeable height differences. The XRD pattern of Zn anode cycled in DP-0 electrolyte exhibits a distinct diffraction peak at 8.3°, which corresponds to ZSH byproducts (Fig. S29). In contrast, no extraneous signals except the characteristic peaks of Zn metal are detected in DP-0.1 electrolyte. Compared to bare Zn, as the cycling time increases, the intensity of (002) plane orientation tendency increases, demonstrating the development of a (002) textured Zn structure (Fig. 4h). Quantitative analysis of the XRD data was performed by calculating the relative texture coefficients (RTCs) using the equation: $\mathrm{RTC}_{(hkl)} = \frac{I_{(hkl)}/I_{0(hkl)}}{\sum I_{(hkl)}/I_{0(hkl)}} \times 100$ where $I_{(hkl)}$ represents the reflection intensity of each crystal plane.[47] As shown in Fig. 4i, the RTC-value of the Zn (002) plane increases from 46.4 to 62.3, while the value of the (100) and (101) planes decreases from 35 to 27 and 18.4 to 10.7, respectively. These results quantitatively validate the emergence of a preferred (002) orientation in the Zn anode when cycled with the DP-0.1 electrolyte. DFT calculations (Fig. S30) indicate that DP molecules preferentially adsorb on the (100) and (101) facets, thereby exposing the (002) facet and promoting growth along the (002) direction.

The *in situ* EIS plots illustrated the evolution of interfacial electrochemical processes over 20 cycles. As shown in Fig. S31, the DP-0.1 expedited rapid stabilization of the charge transfer (R_{ct}) during initial cycles, attributed to preferential adsorption of DP at the interface and the formation of a uniform SEI, which ensures the continued stability of the interface. In contrast, the fluctuating R_{ct} in DP-0 indicates uneven Zn deposition and continued deterioration of the electrode–electrolyte interface. The DRT curves obtained from EIS can be resolved into contributions from Zn^{2+} adsorption (R_{ads}), migration (R_{mig}), charge transfer (R_{ct}), and diffusion (R_{dif}), appearing in order at increasing relaxation times.[48] The impedance values associated with each τ in DP-0 fluctuated significantly, indicating unstable changes in electrode–electrolyte interface (Fig. 4j). The stable impedance values across the four-time constants (τ) in the DP-0.1 electrolyte throughout the cycling process (Fig. 4k) display consistently stable electrode interfacial dynamics. After 20 cycles, the relaxation times of the DP-0 and DP-0.1 electrolyte are 0.9 s and 0.78 s, respectively, which proves that the formation of SEI significantly increased the diffusion rate of Zn^{2+}.

Fig. 5a and Fig. S32 illustrate the reversibility of Zn plating/stripping in Zn||Cu asymmetric cells with/without DP additives. The cells utilizing the DP-0.1 electrolyte exhibit cycling stability over 800 cycles at 1 mA cm^{-2} with a charge of 0.5 mAh cm^{-2}, achieving an average coulombic efficiency (CE) of 99.7%. The comparatively low CE during the initial cycles possibly originates from the consumption of active Zn^{2+} for Cu interface activation. In contrast, Zn||Cu cells with DP-0 electrolyte suffer from rapid cell failure and poor CE. The higher polarization voltage observed in Zn||Cu cells with DP-0.1 (Fig. 5b) is attributed to the adsorption of DP at the anode/electrolyte interface, which modulates Zn nucleation behavior and facilitates uniform Zn deposition. To further elucidate Zn reversibility, a "reservoir half-cell" protocol was employed to quantitatively assess the CE of Zn^{2+} stripping/plating (Fig. 5c).[49,50] Initially, Zn||Cu cells underwent an activation phase comprising two cycles at 1 mA cm^{-2} with an areal capacity of 5 mAh cm^{-2} to mitigate substrate effects. Subsequently, 5 mAh cm^{-2} of Zn (Q_P) was electroplated onto the Cu substrate to establish a Zn reservoir, followed by cycling at 1 mA cm^{-2} with a capacity of 1 mAh cm^{-2} (Q_c). After 20 cycles, a full charge to 0.5 V was applied to strip all Zn (Q_s). Based on the average CE (CE_{avg}) calculation inserted in Fig. 5c, the cell with the DP-0.1 electrolyte achieves a CE_{avg} of 99.1%, higher than that of the cell with the DP-0 electrolyte, confirming the superiority of DP on suppressing side reactions and ensuring highly reversible Zn plating/stripping. The effect of DP on rate performance was evaluated by gradually increasing the current density in steps. Zn||Zn symmetric cell with DP-0.1 exhibits stable voltage

Published on 18 July 2025. Downloaded by Yunnan University on 8/2/2025 10:13:48 PM.

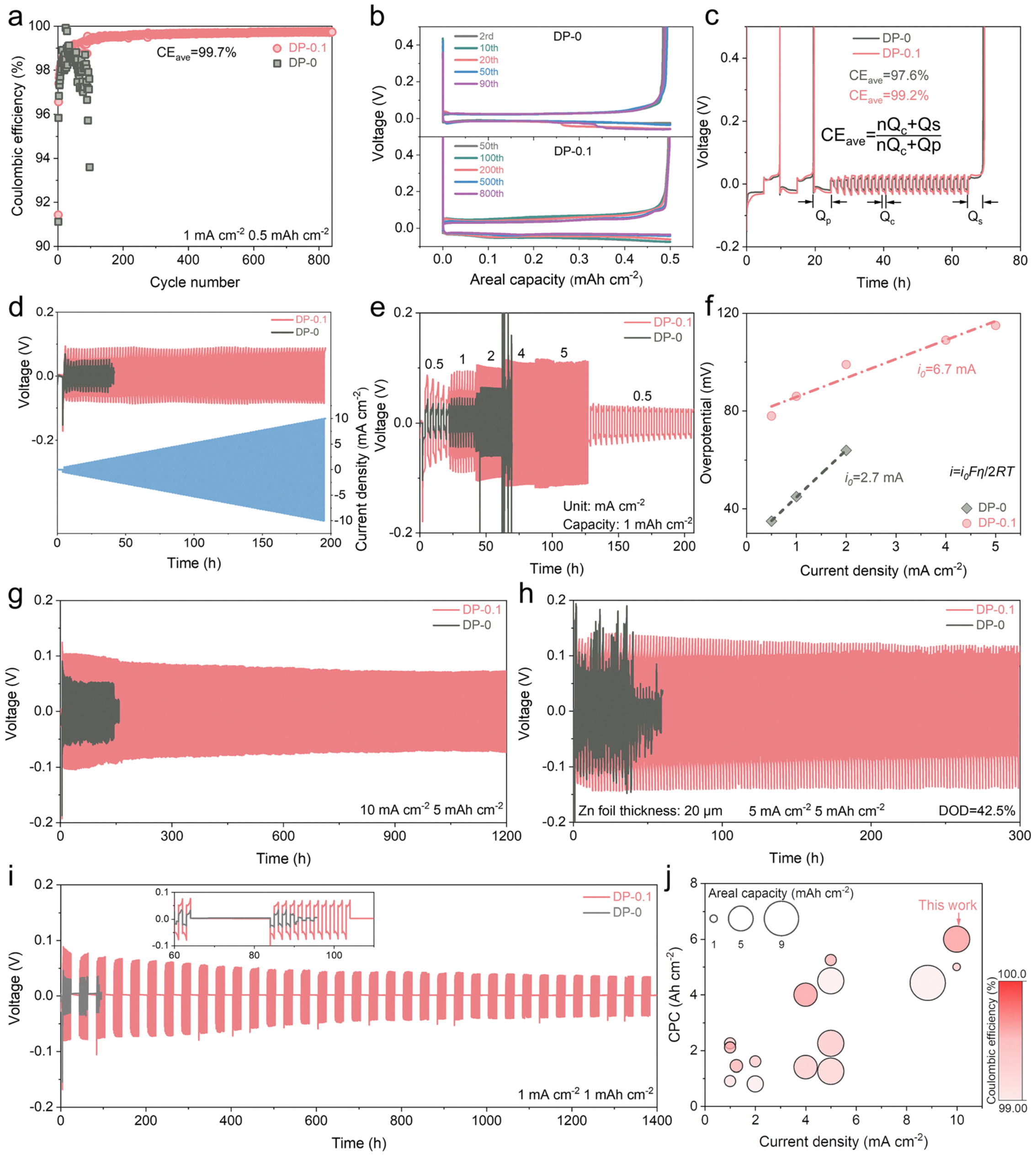

Fig. 5 Electrochemical performance of cells with DP-0 and DP-0.1 electrolytes. (a) CE of Zn||Cu asymmetric cells. (b) The corresponding voltage profiles at various cycles. (c) CE measurement of Zn||Cu cells with the "reservoir" protocol. (d) Potential evolution with stepwise increase of current density. (e) Rate performance of symmetric cells at different current densities with 1 mAh cm^{-2}. (f) Exchange current density. (g) Cycling performance of Zn||Zn symmetric cells at 10 mA cm^{-2} and 5 mAh cm^{-2}. (h) Cycling performance at a high DOD (5 mA cm^{-2} and 5 mAh cm^{-2}). (i) Cycling performance with resting process. (j) Comparison of the CE and CPC with recently reported electrolyte additives.

hysteresis up to 10 mA cm^{-2} (Fig. 5d), indicating enhanced Zn^{2+} diffusion kinetics and improved interfacial stability.

In contrast, cells without DP exhibited substantial voltage fluctuations under high current densities. When the current density was increased from 0.5 to 5 mA cm^{-2}, and then reverted to 0.5 mA cm^{-2} at a fixed areal capacity of 1 mAh cm^{-2}, the Zn||Zn symmetric cells with DP additives demonstrated excellent stability. In contrast, the cell with DP-0 electrolyte short-circuited at 2 mA cm^{-2} (Fig. 5e and Fig. S33). The exchange current density of the Zn anode in the DP-0.1 electrolyte is determined to be 6.7 mA cm^{-2}, higher than the 2.7 mA cm^{-2} measured in DP-0 electrolyte (Fig. 5f), demonstrating the enhancement in Zn nucleation kinetics and ion transport dynamics conferred by DP.

As illustrated in Fig. 5g, Zn||Zn symmetric cell using DP-0 electrolyte suffers short-circuiting after ∼145 h at 10 mA cm^{-2} and 5 mAh cm^{-2}. In contrast, the cell with the DP-0.1 electrolyte maintains stable operation for over 1200 h, achieving a cumulative Zn plating capacity (CPC) of 6 Ah cm^{-2}. A thin Zn foil (20 μm) was employed to evaluate cycle stability under high

This journal is © The Royal Society of Chemistry 2025

Published on 18 July 2025. Downloaded by Yunnan University on 8/2/2025 10:13:48 PM.

depth-of-discharge (DOD) conditions. As shown in Fig. 5h, the Zn||Zn cell with DP-0.1 exhibits a cycling performance of 300 h at 5 mA cm^{-2} with 5 mAh cm^{-2} (42.5% DOD), while the cell with the DP-0 electrolyte exhibits voltage fluctuations and fails after only 50 h. To emulate practical operating conditions, shelf recovery tests were performed. Zn||Zn cells were operated at 1 mA cm^{-2} with 1 mAh cm^{-2}, followed by a 20 h shelving period after every 10 cycles (Fig. 5i). The cell with DP-0.1 electrolyte demonstrated excellent long-term stability, operating for over 1400 h, while the counterpart with DP-0 failed after ~180 h, suggesting that the DP additive effectively inhibits side reactions and preserves electrochemical stability during prolonged cycling. When compared with recently reported electrolyte additives for aqueous ZIBs (Fig. 5j), DP exhibits superior performance in critical parameters such as current density, areal capacity, CPC, and CE, demonstrating the potential of DP as an effective electrolyte additive for advancing the practical applications of high-performance ZIBs.[17,39,51–62]

To investigate the practical application of the DP additive, Zn||NVO full cells were assembled using $NH_4V_4O_{10}$ (NVO) as the cathode material. The NVO cathode materials were uniformly grown on carbon cloth substrates (Fig. S34), as confirmed by XRD analysis (Fig. S35), which showed characteristic peaks that nicely matched the standard PDF card of $NH_4V_4O_{10}$ (JCPDS: 31-0075).[63] As shown in Fig. S36, the Zn||NVO full cell with DP-0.1 electrolyte demonstrates reduced voltage gaps between the V^{5+}/V^{4+} and V^{4+}/V^{3+} redox peaks in the CV curves at a scan rate of 1 mV s^{-1} compared to the cell with DP-0 electrolyte, suggesting enhanced reversibility and accelerated reaction kinetics facilitated by the DP additive. For the voltage profiles at a current density of 0.1 A g^{-1} (Fig. S37), the lower voltage gap in the DP-0.1 compared to the DP-0 electrolyte (255 mV *vs.* 270 mV) further confirms its enhanced reversibility. As shown in Fig. 6a, rate capability reveals comparable initial capacities of both cells at 0.5 A g^{-1} (330 mAh g^{-1} for DP-0 and 335 mAh g^{-1} for DP-0.1, respectively). The full cell with DP-0.1 electrolyte exhibits a high capacity of 215 mAh g^{-1} at 5 A g^{-1}, surpassing its counterpart (171 mAh g^{-1} at 5 A g^{-1}). When the current density returns to 0.5 A g^{-1}, the capacity recovers to 332 mAh g^{-1}. The cycling performance at a low current density of 0.2 A g^{-1} is shown in Fig. S38. The initial capacity of Zn||NVO with DP-0.1 electrolyte reaches 357 mAh g^{-1} and retains 298 mAh g^{-1} after 1000 cycles, corresponding to an

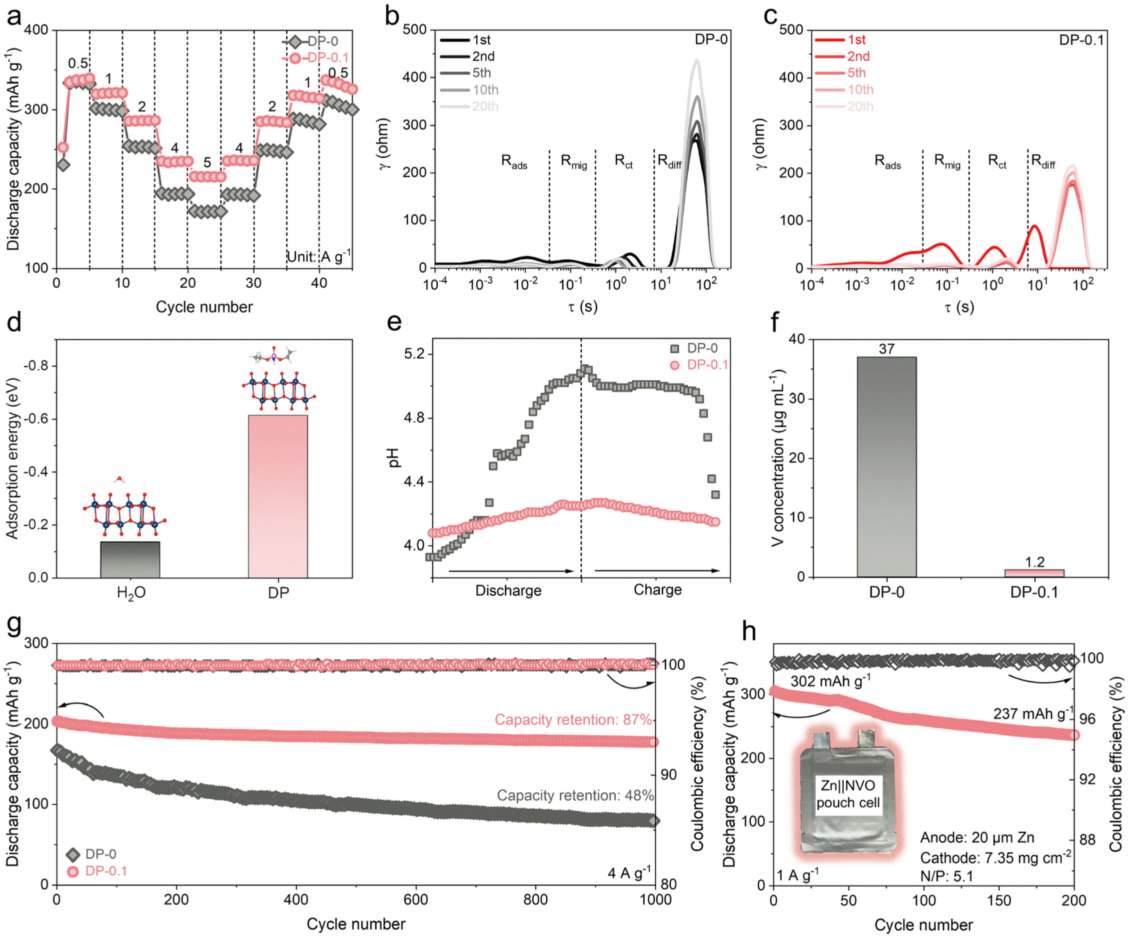

Fig. 6 Electrochemical properties and practical application of Zn||NVO full cells with DP-0 and DP-0.1 electrolytes. (a) Rate capability. DRT of Zn||NVO full cells with (b) DP-0 and (c) DP-0.1 electrolytes after various cycles. (d) Adsorption energy of DP and H_2O on the (001) plane of the NVO cathode. (e) pH evolution at the cathode/electrolyte interface. (f) V concentration of electrolytes after immersion. (g) Cycling performance at 4 A g^{-1}. (h) Cycling performance of the Zn||NVO pouch cells with DP-0.1 electrolyte.

Published on 18 July 2025. Downloaded by Yunnan University on 8/2/2025 10:13:48 PM.

83.5% capacity retention, superior to that with DP-0 electrolyte (42.3%). The DRT curves derived from *in situ* EIS test during cycling (Fig. 6b and c) reveal that the full cell employing the DP-0.1 electrolyte maintains a stable impedance profile, suggesting its superior capability to modulate the electrochemical environment. In contrast, cells with the DP-0 electrolyte exhibit a gradual increase in resistance, indicating the fluctuations in the internal electrochemical environment. After 20 cycles, the integrated areas corresponding to both charge transfer and diffusion processes in the Zn||NVO cell with the DP-0.1 electrolyte are reduced compared to those with the DP-0 electrolyte, indicating that the electrode reactions are both rapid and highly reversible. The mechanism of stable interface is investigated by DFT calculation (Fig. 6d). The results show that the absorption energy of the DP on the NVO cathode is −0.614 eV, higher than that of water molecules (−0.134 eV), indicating the preferential adsorption of DP on the NVO cathode to form a DP-enriched dynamic CEI. XPS, FTIR, Raman, and HRTEM were used to further characterize the CEI. XPS spectra of the NVO cathode cycled in DP-0.1 electrolyte exhibit distinct P═O and $-NH_2$ signals (Fig. S39). FTIR and Raman spectra (Fig. S40 and S41) also show the characteristic peaks originating from the adsorbed DP. HRTEM image (Fig. S42) reveals that the ultrathin CEI (less than 5 nm in thickness) is transformed on the surface of the NVO after cycling in DP-0.1. The crystal lattice in the CEI could be attributed to the plane of $Zn_3(PO_4)_2$. As shown in Fig. 6e, in the DP-0 electrolyte, the cathodic interfacial pH exhibits significant fluctuations during charge and discharge, indicating proton transfer and possible parasitic reactions that can accelerate the degradation of cathode materials. In contrast, the self-adaptive CEI effectively suppresses interfacial pH fluctuations due to the buffering capability of DP, maintaining a stable electrochemical interface and inhibiting dissolution. The electrodes were immersed in $ZnSO_4$ electrolytes with and without the DP additive for 5 days, as shown in Fig. 6f. The DP-0 electrolyte exhibited a noticeable yellowish color with a V concentration of 37 $\mu g\ mL^{-1}$. In contrast, the electrolyte containing DP remained transparent (Fig. S43), confirming the dissolution of vanadium species from the cathode material in the absence of DP. The Zn||NVO full cell with DP-0.1 electrolyte displays a low E_a of 24.3 kJ mol^{-1}, compared to 28.2 kJ mol^{-1} for that with DP-0 electrolyte (Fig. S44), suggesting the fast desolvation process at the interface. The galvanostatic intermittent titration technique (GITT) results (Fig. S45) reveal that the Zn^{2+} diffusion coefficient of NVO in DP-0.1 electrolyte is higher than that in DP-0 electrolyte, indicating the fast ions migration in the bulk structure. These results indicate that the DP layer can repel free water and accelerate the desolvation of hydrated Zn^{2+}, thus effectively suppressing the cathode dissolution and enabling fast ion (de)intercalation.

Self-discharge behaviors were evaluated through open-circuit potential monitoring after 24 hours of storage at a fully charged state (Fig. S46). The cell with DP-0.1 electrolyte maintains a stable open-circuit potential of 1.01 V with a CE of 88.9%, outperforming the DP-0 counterpart (0.98 V and 72.5%) due to the effective suppression of side reactions and the inhibited dissolution of the NVO cathode by the DP additive. Long-term cycling performance (Fig. 6g) demonstrates that the Zn||NVO full cell with DP-0.1 electrolyte achieved 83% capacity retention over 1000 cycles at 4 A g^{-1}, compared to only 48% retention for the cell using DP-0 electrolyte. The surface morphology and crystalline structure of both the NVO cathode and the Zn anode after cycling were examined. The Zn anode cycled with DP-0 electrolyte exhibits extensive dendritic growth, whereas the anode in the DP-0.1 electrolyte retains a smooth, dense morphology with no significant dendrite formation (Fig. S47). Similarly, the NVO cathode in the DP-0 electrolyte suffers from severe structural collapse and dissolution of active material. In contrast, the integrity of the cathode structure is preserved in the presence of the DP additive (Fig. S48). XRD patterns of the cycled Zn anode (Fig. S49) further reveal the formation of corrosion products in the DP-0 electrolyte. The NVO in DP-0.1 electrolyte maintains the original crystalline structure. In contrast, the weak diffraction peaks of NVO and the byproducts generated in the DP-0 electrolyte are attributed to structural degradation and proton intercalation (Fig. S50). Based on the above analysis, the suppression of vanadium dissolution, proton intercalation, and byproducts formation is responsible for the high rate capability and long cycling lifespan. Practical application potential was further evaluated using a 4 × 5 cm^{-1} pouch cell, where the Zn||NVO full cell with DP-0.1 electrolyte exhibits a capacity of 237 mAh g^{-1} after 200 cycles at 1 A g^{-1} (Fig. 6h). With a low N/P ratio of 3.2, the assembled Zn||NVO pouch cell with DP-0.1 electrolyte operated stably for 100 cycles with a capacity retention of 87.8% (Fig. S51). The successful operation of a thermometer powered by the Zn||NVO pouch cell with DP-0.1 electrolyte (Fig. S52) highlights the commercial viability of this system for aqueous ZIBs.

Conclusion

The introduction of DP demonstrates its capability to optimize anode/electrolyte and cathode/electrolyte interfacial chemistry and to buffer pH fluctuations. The DP molecules disrupt the water hydrogen-bonding network and adsorb onto the Zn surface, inducing the *in situ* formation of a robust crystalline–amorphous hybrid SEI layer comprising ZnS, Zn_3N_2, and $Zn_3(PO_4)_2$, resulting in the suppression of dendrite growth and side reactions. The formation of a dynamic DP-rich CEI on the cathode surface prevents the dissolution of vanadium-based materials by polar water molecules, promoting intercalation stability and reversibility. As a result, the Zn||Zn symmetric cell exhibits an enhanced lifespan of 1200 h at a current density of 10 mA cm^{-2} and an areal capacity of 5 mAh cm^{-2}, and the Zn||Cu asymmetric cell maintains an average CE of 99.7% over 800 cycles at 1 mA cm^{-2} and 0.5 mAh cm^{-2}. Besides, the Zn||NVO full cell demonstrates an improved cycling stability (87% capacity retention after 1000 cycles at 4 A g^{-1}), and the assembled pouch cell also stably operates for over 200 cycles.

This journal is © The Royal Society of Chemistry 2025

Published on 18 July 2025. Downloaded by Yunnan University on 8/2/2025 10:13:48 PM.

Conflicts of interest

There are no conflicts to declare.

Data availability

The data supporting this article have been included as part of the SI.

Experimental section, the characterizations of electrolytes and Zn anode, the cycling performance and the characterizations of full cells. See DOI: https://doi.org/10.1039/d5ee02236c

Acknowledgements

This work was supported by Zhejiang Provincial Natural Science Foundation of China (Grant No. LQ24E020004), the National Natural Science Foundation of China (Grant No. 52302322), the Fundamental Research Funds for the Provincial Universities of Zhejiang (2024YW13), and the Zhejiang Province Postdoctoral Research Project (ZJ 2024040).

References

1 S. Lei, Z. Liu, C. Liu, J. Li, B. Lu, S. Liang and J. Zhou, *Energy Environ. Sci.*, 2022, **15**, 4911–4927.
2 Z. Ju, Q. Zhao, D. Chao, Y. Hou, H. Pan, W. Sun, Z. Yuan, H. Li, T. Ma, D. Su and B. Jia, *Adv. Energy Mater.*, 2022, **12**, 2201074.
3 M. Song, H. Tan, D. Chao and H. J. Fan, *Adv. Funct. Mater.*, 2018, **28**, 1802564.
4 X. Jia, C. Liu, Z. G. Neale, J. Yang and G. Cao, *Chem. Rev.*, 2020, **120**, 7795–7866.
5 L. Tang, H. Peng, J. Kang, H. Chen, M. Zhang, Y. Liu, D. H. Kim, Y. Liu and Z. Lin, *Chem. Soc. Rev.*, 2024, **53**, 4877–4925.
6 Z. Ju, T. Zheng, B. Zhang and G. Yu, *Chem. Soc. Rev.*, 2024, **53**, 8980–9028.
7 X. Yu, Z. Li, X. Wu, H. Zhang, Q. Zhao, H. Liang, H. Wang, D. Chao, F. Wang, Y. Qiao, H. Zhou and S.-G. Sun, *Joule*, 2023, **7**, 1145–1175.
8 J. Hao, X. Li, X. Zeng, D. Li, J. Mao and Z. Guo, *Energy Environ. Sci.*, 2020, **13**, 3917–3949.
9 X. Li, P. Liu, C. Han, T. Cai, Y. Cui, W. Xing and C. Zhi, *Energy Environ. Sci.*, 2025, **18**, 2050–2094.
10 H. Li, S. Li, R. Hou, Y. Rao, S. Guo, Z. Chang and H. Zhou, *Chem. Soc. Rev.*, 2024, **53**, 7742–7783.
11 R. Sinha, X. Xie, Y. Yang, Y. Li, Y. Xue, P. Wang and Z. Li, *Adv. Energy Mater.*, 2025, **15**, 2404815.
12 Y. Dai, C. Zhang, J. Li, X. Gao, P. Hu, C. Ye, H. He, J. Zhu, W. Zhang, R. Chen, W. Zong, F. Guo, I. P. Parkin, D. J. L. Brett, P. R. Shearing, L. Mai and G. He, *Adv. Mater.*, 2024, **36**, 2310645.
13 T. Wang, S. Tang, Y. Xiao, W. Xiang and J. S. Yu, *Energy Environ. Sci.*, 2025, **18**, 545–578.
14 Y.-P. Deng, R. Liang, G. Jiang, Y. Jiang, A. Yu and Z. Chen, *ACS Energy Lett.*, 2020, **5**, 1665–1675.
15 J. Cao, X. Wang, S. Qian, D. Zhang, D. Luo, L. Zhang, J. Qin, X. Zhang, X. Yang and J. Lu, *Adv. Mater.*, 2024, **36**, 2410947.
16 D. Wang, S. Hu, T. Li, C. Chang, S. Li, S. Guo, H. Li, Q. Liu, J. Gong, J. Zhou and C. Han, *Nat. Commun.*, 2025, **16**, 259.
17 H. Huang, J. Xu, Y. Huang, Z. He, H. Feng, C. Hu, Z. Chen, Z. Yang, T. Tian and W. Zhang, *Adv. Energy Mater.*, 2024, **14**, 2401643.
18 Y. Xu, X. Zhou, Z. Chen, Y. Hou, Y. You and J. Lu, *Mater. Today*, 2023, **66**, 339–347.
19 W. Chen, Y. Wang, F. Wang, Z. Zhang, W. Li, G. Fang and F. Wang, *Adv. Mater.*, 2024, **36**, 2411802.
20 Y. Li, Z. Yu, J. Huang, Y. Wang and Y. Xia, *Angew. Chem., Int. Ed.*, 2023, **62**, e202309957.
21 D. Wang, Q. Li, Y. Zhao, H. Hong, H. Li, Z. Huang, G. Liang, Q. Yang and C. Zhi, *Adv. Energy Mater.*, 2022, **12**, 2102707.
22 Y. Zeng, D. Luan and X. W. Lou, *Chem*, 2023, **9**, 1118–1146.
23 B. Yong, D. Ma, Y. Wang, H. Mi, C. He and P. Zhang, *Adv. Energy Mater.*, 2020, **10**, 2002354.
24 K. Zhu, T. Wu and K. Huang, *Chem. Mater.*, 2021, **33**, 4089–4098.
25 D. Zhang, J. Cao, X. Zhang, N. Insin, S. Wang, J. Han, Y. Zhao, J. Qin and Y. Huang, *Adv. Funct. Mater.*, 2021, **31**, 2009412.
26 X. Zhang, X. Ma, H. Bi, Y. Zhang, P. Mi, F. Liu, X. Jin, Y. Chen, K. Zhang, J. Wang and Y. Dong, *Adv. Funct. Mater.*, 2024, **35**, 2411990.
27 S. Wei, S. Chen, X. Su, Z. Qi, C. Wang, B. Ganguli, P. Zhang, K. Zhu, Y. Cao, Q. He, D. Cao, X. Guo, W. Wen, X. Wu, P. M. Ajayan and L. Song, *Energy Environ. Sci.*, 2021, **14**, 3954–3964.
28 Z. Jia, X. Yang, H. Y. Shi, S. Hu and X. Sun, *Chem. Commun.*, 2022, **58**, 5905–5908.
29 L. Lin, Z. Shao, S. Liu, P. Yang, K. Zhu, W. Zhuang, C. Li, G. Guo, W. Wang, G. Hong, B. Wu, Q. Zhang and Y. Yao, *Angew. Chem., Int. Ed.*, 2025, **64**, e202425008.
30 Z. Yang, Y. Sun, S. Deng, H. Tong, M. Wu, X. Nie, Y. Su, G. He, Y. Zhang, J. Li and G. Chai, *Energy Environ. Sci.*, 2024, **17**, 3443–3453.
31 A. Wu, S. Zhang, Q. Li, W. Xue, C. Li, B. Xi, W. Mao, K. Bao and S. Xiong, *Adv. Energy Mater.*, 2025, **15**, 2404450.
32 P. Wang, T. C. Li, Y. Liu, C. Lin, Y. Cui, H. Song, B. Lu, S. Liang, H. Y. Yang and J. Zhou, *Angew. Chem., Int. Ed.*, 2025, **137**, e202422547.
33 Y. Xu, K. Chen, M. Xu, Y. Li, Q. Wu, S. Li, C. Xie, Y. Li, H. Xie and J. Huang, *Energy Environ. Sci.*, 2025, **18**, 1560–1571.
34 D. Li, C. Li, W. Liu, H. Bu, X. Zhang, T. Li, J. Zhang, M. Kong, X. Wang, C. Wang and X. Xu, *Adv. Funct. Mater.*, 2024, **35**, 2415107.
35 C. Li, X. Zhang, G. Qu, S. Zhao, H. Qin, D. Li, N. Li, C. Wang and X. Xu, *Adv. Energy Mater.*, 2024, **14**, 2400872.
36 J. Chen, G. Ou, P. Liu, W. Fan, B. Li, Z. Hu, Z. Wen, Y. Zhang, Y. Tang, X. Liu, M. Ye and C. C. Li, *Angew. Chem., Int. Ed.*, 2025, **64**, e202414166.
37 J. Bu, P. Liu, G. Ou, M. Ye, Z. Wen, Y. Zhang, Y. Tang, X. Liu and C. C. Li, *Adv. Mater.*, 2025, **37**, 2420221.

This journal is © The Royal Society of Chemistry 2025

Published on 18 July 2025. Downloaded by Yunnan University on 8/2/2025 10:13:48 PM.

38 Z. Guo, Z. Liu, P. Wang, C. Zhao, X. Lu, Y. Zhang and N. Zhang, *Nano Lett.*, 2024, **24**, 14656–14662.

39 Q. Deng, S. You, W. Min, Y. Xu, W. Lin, J. Lu and C. Yang, *Adv. Mater.*, 2024, **36**, 2312924.

40 K. Yang, H. Fu, Y. Duan, Z. Ma, D. Wang, B. Li, H. S. Park and D. Ho, *ACS Energy Lett.*, 2023, **9**, 209–217.

41 H. Yang, K. Zhu, W. Xie and W. Yang, *ACS Nano*, 2025, **19**, 1433–1446.

42 X. Liu, W. Zhang, Y. Liu, X. Li, D. Zhang, K. Wang, L. Liu and C. Huang, *Energy Environ. Sci.*, 2024, **17**, 9538–9547.

43 W. Zhang, R. Chen, Y. Dai, X. Wu, J. Chen, W. Zong, M. Zhang, Z. Du, H. Dong, F. Zhao, H. Yang, J. Borowiec, Z. Xu, Z. Li, M. Liu, G. He and I. P. Parkin, *Mater. Today*, 2024, **78**, 32–45.

44 J. Weng, W. Zhu, K. Yu, J. Luo, M. Chen, L. Li, Y. Zhuang, K. Xia, Z. Lu, Y. Hu, C. Yang, M. Wu and Z. Zou, *Adv. Funct. Mater.*, 2024, **34**, 2314347.

45 M. Kim, J. Lee, Y. Kim, Y. Park, H. Kim and J. W. Choi, *J. Am. Chem. Soc.*, 2023, **145**, 15776–15787.

46 S. Huang, P. Zhang, J. Lu, J. S. Kim, D. H. Min, J. S. Byun, M. J. Kim, H. Fu, P. Xiong, P. J. Yoo, W. Li, X. Yu, X. Qin and H. S. Park, *Energy Environ. Sci.*, 2024, **17**, 7870–7881.

47 H. Zhang, Y. Zhong, J. Li, Y. Liao, J. Zeng, Y. Shen, L. Yuan, Z. Li and Y. Huang, *Adv. Energy Mater.*, 2022, **13**, 2203254.

48 J. Huang, Y. Zhong, H. Fu, Y. Zhao, S. Li, Y. Xie, H. Zhang, B. Lu, L. Chen, S. Liang and J. Zhou, *Adv. Mater.*, 2024, **36**, 2406257.

49 G. Ma, W. Yuan, X. Li, T. Bi, L. Niu, Y. Wang, M. Liu, Y. Wang, Z. Shen and N. Zhang, *Adv. Mater.*, 2024, **36**, 2408287.

50 Q. Li, D. Luo, Q. Ma, Z. Zheng, S. Li, Y. Xie, L. Xue, M. Lin, Y. Nie, G. Feng, H. Dou, J. Chen, X. Wang and Z. Chen, *Energy Environ. Sci.*, 2025, **18**, 1489–1501.

51 Q. Nian, X. Luo, D. Ruan, Y. Li, B. Q. Xiong, Z. Cui, Z. Wang, Q. Dong, J. Fan, J. Jiang, J. Ma, Z. Ma, D. Wang and X. Ren, *Nat. Commun.*, 2024, **15**, 4303.

52 H. B. Chen, H. Meng, T. R. Zhang, Q. Ran, J. Liu, H. Shi, G. F. Han, T. H. Wang, Z. Wen, X. Y. Lang and Q. Jiang, *Angew. Chem., Int. Ed.*, 2024, **63**, e202402327.

53 Z. Luo, Y. Xia, S. Chen, X. Wu, E. Akinlabi, B. B. Xu, H. Pan, M. Yan and Y. Jiang, *Energy Environ. Sci.*, 2024, **17**, 6787–6798.

54 Z. Cheng, K. Wang, J. Fu, F. Mo, P. Lu, J. Gao, D. Ho, B. Li and H. Hu, *Adv. Energy Mater.*, 2024, **14**, 2404003.

55 R. Han, T. Jiang, Z. Wang, R. Xue, X. Liu, Y. Tang, Z. Qi and Y. Ma, *Adv. Funct. Mater.*, 2024, **35**, 2412255.

56 L. Zheng, H. Li, X. Wang, Z. Chen, C. Hu, K. Wang, G. Guo, S. Passerini and H. Zhang, *ACS Energy Lett.*, 2023, **8**, 2086–2096.

57 L. Liu, X. Wang, Z. Hu, X. Wang, Q. Zheng, C. Han, J. Xu, X. Xu, H. K. Liu, S. X. Dou and W. Li, *Angew. Chem., Int. Ed.*, 2024, **63**, e202405209.

58 X. Wang, K. Feng, B. Sang, G. Li, Z. Zhang, G. Zhou, B. Xi, X. An and S. Xiong, *Adv. Energy Mater.*, 2023, **13**, 2301670.

59 N. Hu, W. Lv, W. Chen, H. Tang, X. Zhang, H. Qin, D. Huang, J. Zhu, Z. Chen, J. Xu and H. He, *Adv. Funct. Mater.*, 2023, **34**, 2311773.

60 H. Yu, D. Chen, X. Ni, P. Qing, C. Yan, W. Wei, J. Ma, X. Ji, Y. Chen and L. Chen, *Energy Environ. Sci.*, 2023, **16**, 2684–2695.

61 H. Wang, Y. Liu, M. Zhu, Y. Chen, D. Chen, Z. Lin, K. Wang, Z. Xu, S. Chen, G. Xing, O. I. Malyi, Y. Tang and Y. Zhang, *Angew. Chem., Int. Ed.*, 2025, **64**, e202414473.

62 G. Gao, X. Huo, B. Li, J. Bi, Z. Zhou, Z. Du, W. Ai and W. Huang, *Energy Environ. Sci.*, 2024, **17**, 7850–7859.

63 S. Li, X. Xu, W. Chen, J. Zhao, K. Wang, J. Shen, X. Chen, X. Lu, X. Jiao, Y. Liu and Y. Bai, *Energy Storage Mater.*, 2024, **65**, 103108.

This journal is © The Royal Society of Chemistry 2025